Numerical Study on the Effects of Propellant Species in a Self-Field Magnetoplasmadynamic Arcjet

IEPC-2009-232

Presented at the 31st International Electric Propulsion Conference,
University of Michigan • Ann Arbor, Michigan • USA
September 20 – 24, 2009

H. Sato[1]
The Graduate University for Advanced Studies, Sagamihara, Kanagawa, 229-8510, Japan

K. Kubota[2] and I. Funaki[3]
Japan Aerospace Exploration Agency, Sagamihara, Kanagawa, 229-8510, Japan

Abstract: Numerical simulation of the plasma flow in a self-field MPD thruster with flared anode configuration was conducted. Hydrogen is adopted as a propellant because of its widely-known potential for efficient operation. The mass flow rate is set at 1.37 g/s, and the discharge current is varied from 5 to 13 kA, which results in a power range of 216 kW-1.45 MW, a thrust of 18.9 – 38.5 N, and a specific impulse of 1443 - 2856 s. The calculated thrust characteristic is almost the same as the measured thrust over the calculated discharge current range. At 13 kA, the maximum degrees of dissociation and ionization reach 0.88 and 0.87 within the cathode jet. It is also shown that the current contour lines are obliquely distorted due to the Hall effect, and the extent of the distortion is significantly enlarged by decreasing the electron temperature on the anode. From the analysis of the energy balance at the thruster exit, it is found that the frozen flow loss is dominant (dissociation and ionization energy).

Nomenclature

$\mathbf{B}$	=	magnetic flux density, T
$\mathbf{E}$	=	electric field, V/m
e	=	elementary charge (= 1.6×10^{-19}, C)
F	=	thrust, N
$\mathbf{I}$	=	Unit tensor
I_{sp}	=	Specific impulse, s
J	=	Total discharge current, A
$\mathbf{j}$	=	current density, A/m^2
k_{bol}	=	Boltzmann constant
k	=	reaction rate constant
m	=	Molecular weight
n	=	number density, m^{-3}
p	=	pressure, Pa
Q_{e-T}	=	electron-heavy energy exchange
$\mathbf{q}$	=	heat flux, W/m^2

[1] Graduate Student, Department of Space and Astronautical Science, E-mail: satoh.hiroki@jaxa.jp
[2] Research Fellow of JSPS, Institute of Space and Astronautical Science, E-mail: kubota.kenichi@jaxa.jp
[3] Associate Professor, Institute of Space and Astronautical Science, E-mail: funaki@isas.jaxa.jp

r = radial coordinate
T = temperature, K
U = internal energy, J/m^3
$\mathbf{u}$ = velocity, km/s
V_{ion} = ionization energy, eV
V_{diss} = dissociation energy, eV
V = voltage, V
z = axial coordinate
α = ionization fraction, -
η = thrust efficiency, %
λ = thermal conductivity, W/(m・K)
μ_0 = permeability
μ = viscous coefficient, m^2/s
ρ = mass density, kg/m^3
σ = electrical conductivity, S/m
τ = viscous stress tensor
Φ = dissipation function

Subscript

b = backward
D = Dissociation
dis = discharge current
e = electron
f = forward
gas = gasdynamic thrust component
h = heavy particle
H_2 = hydrogen molecular
H = hydrogen atom
H^+ = hydrogen ion
i = inlet
I = Ionizaiton
mag = electromagnetic thrust component
s = s specie
th = thrust

I. Introduction

In a self-field magnetoplasmadynamic thruster (MPDT), the Lorentz force obtained from the discharge current and the induced magnetic field accelerates a plasma produced by arc discharge, as shown in Fig. 1. The advantages of MPDTs are simple structure and high thrust density which is required for a manned space mission in the future.

Although many experimental and theoretical researches on MPDT have been reported over the past four decades, MPDT has not yet become a practical thruster due to its low thrust efficiency. In the basic study, MPDTs with argon propellant have been studied experimentally and numerically[13-15] by many researchers. Typically measured maximum thrust efficiency was about 20%.[16-19] Thrust efficiency, however, might be improved by selecting proper propellant species. For example, the maximum thrust efficiency of MPDTs using hydrogen propellant reaches over 50%.[1, 16] Since there remains a problem of storage system for hydrogen, hydrogen compound such as hydrazine N_2H_4 may be practical. However, as a first step, it will be meaningful to develop a numerical tool for MPDTs with hydrogen propellant. There have been some numerical studies on hydrogen MPDT,[2, 3, 6, 20, 21] discussions on flowfields taking account of all of the realistic effects (e.g. chemical non-equilibrium processes of dissociation and ionization, Hall effect, viscous, and thermal conductivity) have not been carried out in detail.

Our final goals are to develop a numerical simulation tool for MPDT using a propellant of hydrogen compound (e.g. NH_3 and N_2H_4), and to obtain an insight for high thrust efficiency, but in this study, we limit our discussion to pure H_2 propellant as a preliminary step. Magnetohydrodynamic (MHD) simulation with real gas effect (e.g. thermal nonequiliburium, dissociation-ionization process, and Hall effect) is conducted in order to quantitatively investigate the flow field, the discharge characteristic, and thrust efficiency.

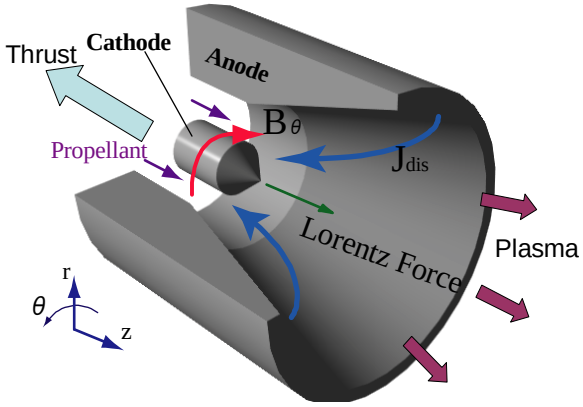

Figure 1. Schematic of Self-field MPD thruster.

II. Physical and Numerical Modeling

A. Assumptions for Modeling

Assumptions in our present model are summarized as follows.

- 2-dimensional axisymmetric flow structure is assumed.
- Non-equilibrium ionization and dissociation processes are incorporated.
- 2-temperature (translational temperature of heavy particle and electron temperature) model is used.
- Rotational and vibrational energy of a molecular are ignored.
- Ion slip and electron pressure gradient are ignored in Ohm's law.

The following reactions (ionization and dissociation) are taken into account.

- Dissociation process

  1) $H_2 + e^- \rightarrow H + H + e^-$

  2) $H_2 + H_2 \rightarrow H + H + H_2$

  3) $H_2 + M \rightarrow H + H + M$ ($M = H, H^+$)
- Ionization process

  4) $H + e^- \rightarrow H^+ + e^- + e^-$

The reaction rate coefficients are referred from Ref. (3).The dissociation energy V_{diss} and ionization energy V_{ion} are 4.4 eV and 13.6 eV, respectively.

B. Basic Equations

The plasma flow in an MPDT is treated with magnetohydrodynamic (MHD) model.

Total mass density

$$\frac{\partial \rho}{\partial t} + \nabla \cdot (\rho \mathbf{u}) = 0 \tag{1}$$

Mass density of atom and ion

$$\frac{\partial \rho_s}{\partial t} + \nabla \cdot (\rho_s \mathbf{u}) = \dot{\rho}_s \qquad (\mathrm{s} = \mathrm{H}, \mathrm{H}^+) \tag{2}$$

Momentum

$$\frac{\partial \rho \mathbf{u}}{\partial t} + \nabla \cdot (\rho \mathbf{u}\mathbf{u} + p\mathbf{I}) = \nabla \cdot \boldsymbol{\tau} + \mathbf{j} \times \mathbf{B} \tag{3}$$

Internal energy of heavy particle (translation)

$$\frac{\partial U_h}{\partial t} + \nabla \cdot (U_h \boldsymbol{u}) = -p_h \nabla \cdot \boldsymbol{u} + \Phi + \nabla \cdot (\lambda \nabla T_h) + Q_{e-T} - \frac{1}{2}\dot{n}_{H,diss}\hat{V}_{diss} \tag{4}$$

Internal energy of electron

$$\frac{\partial U_e}{\partial t} + \nabla \cdot (U_e \mathbf{u}) = -p_e \nabla \cdot \mathbf{u} + \nabla \cdot (\lambda_e \nabla T_e) - Q_{e-T} + \frac{|\mathbf{j}|^2}{\sigma} - \frac{1}{2}\dot{n}_{e,diss}\hat{V}_{diss} - \dot{n}_{e,ion}\hat{V}_{ion} \tag{5}$$

Induction equation

$$\frac{\partial \mathbf{B}}{\partial t} - \nabla \times (\mathbf{u} \times \mathbf{B}) = -\nabla \times \left[\frac{1}{\mu_0 \sigma} \nabla \times \mathbf{B} + \frac{1}{\mu_0 e n_e} (\nabla \times \mathbf{B}) \times \mathbf{B} \right] \tag{6}$$

To close the equations of system, the equation of state is coupled with the above equations:

$$p = \sum_{s \neq e} n_s k_{bol} T_h + n_e k_{bol} T_e = nk\{T_h(1 + \alpha_{diss}) + 2\alpha T_e\} \tag{7}$$

In the right hand of Eq. (2), chemical reaction term $\dot{\rho}_s$ (s = H, H^+) is evaluated as follows[7,8]:

$$\dot{\rho}_H = m_H \left\{ \sum_i \left(k_{DF,i} n_{H_2} - k_{DB,i} n_H n_H \right) n_i - \left(k_{IF} n_H n_e - k_{IB} n_{H^+} n_e n_e \right) \right\} \qquad (\mathrm{i} = \mathrm{e}, \mathrm{H}_2, \mathrm{H}, \mathrm{H}^+) \tag{8}$$

$$\dot{\rho}_{H^+} = m_{H^+} \left(k_{IF} n_H n_e - k_{IB} n_{H^+} n_e n_e \right) \tag{9}$$

In the right hand of Eq. (4), (5), $\dot{n}_{H,diss}, \dot{n}_{e,diss}$ and $\dot{n}_{e,ion}$ are defined as follows.

$$\dot{n}_{H,diss} = \sum_{i \neq e} \left(k_{DF,i} n_{H_2} - k_{DB,i} n_H n_H \right) n_i \tag{10}$$

$$\dot{n}_{e,diss} = k_{DF,e} n_e n_{H_2} - k_{DB,e} n_e n_H n_H \tag{11}$$

$$\dot{n}_{e,ion} = k_{IF} n_H n_e - k_{IB} n_{H^+} n_e n_e \tag{12}$$

In Eq.(7), ideal gas is assumed for each species. α_{diss}, α show dissociation and ionization fraction, respectively, which are defined as follows[9].

$$\alpha_{diss} \equiv \frac{1}{2} \frac{n_H + n_{H^+}}{n} \tag{13}$$

$$\alpha \equiv \frac{1}{2} \frac{n_e}{n} \tag{14}$$

Here, in the case of fully dissociation and ionization, α_{diss}, α is 1.0, respectively. In addition, n in this equation is defined as follows:

$$n \equiv n_{H2} + \frac{1}{2}\left(n_H + n_{H^+} \right) \tag{15}$$

In Eq.(4) and (5), $Q_{e\text{-}T}$ shows the energy exchange due to elastic collision between electrons and heavy particle.[22]

C. Thruster Geometry

In this simulation, the MY-II[1] is employed as the thruster geometry for the validation of a coaxial MPDT. Figure 2 shows the simulated mesh which is divided into two blocks (Thruster and Plume region). The propellant is injected from the propellant port (z = 0 mm, r = 5 – 25 mm) in this simulation.

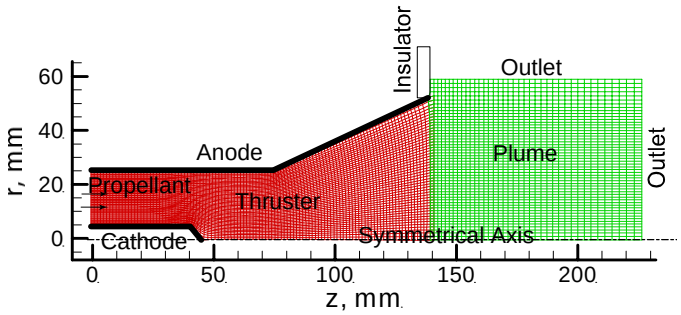

Figure 2. Thruster Geometry and Simulation Region.

D. Numerical Method

The governing Eqs. (1)–(6) in the preceding section are solved numerically by using a time-marching with predictor-corrector method. All equations are solved following second-order Lax–Friedrich total variation diminishing (TVD) scheme. We select the Lax–Friedrich TVD scheme due to its robustness and the fact that it can be easily applied to any system of conservation equations. The finite volume spacial discretization is adopted, and then the numerical flux on the cell surface is calculated using the MUSCL approach[4].

E. Boundary Conditions and Simulation Conditions

The mass flow rate $\dot{m}$, the heavy particle temperature T_h, the electron temperature, the dissociation fraction, and the ionization fraction are set to the values summarized in Table 1. The mass flow rate $\dot{m}$ in this simulation is set to the value used in the experiment conducted by Tahara[1]. The radial distribution of the magnetic flux density at the inlet is obtained from Ampère's law, that is, $B_{in} = -\mu_0 J_{dis}/2\pi r$, where J_{dis} is the total discharge current. Along the walls, non-slip condition is applied for the velocity boundary condition, and both T_h and T_e are obtained from adiabatic condition. At the thruster exit, free-stream condition is employed for all variables.

The magnetic flux density on the electrodes is determined from the equipotential condition, i.e. the electric field along the wall is set to zero. The total discharge current J_{dis} is varied over the range of 5 – 13 kA (9 cases).

Table 1. Simulation Condition for MPDT.

Discharge current (9 cases), kA	5 - 13
Propellant mass flow rate, g/s	1.37
Propellant species	H_2
Heavy particle temp. at inlet, K	4000
Electron temp. at inlet, K	10000
Ionization fraction at inlet	0.01
Dissociation fraction at inlet	0.05
wall	Adiabatic

III. Numerical Results and Discussion

A. Flow Field

Dissociation and Ionization fraction and Electron Density

Figure 3 shows the distribution of dissociation fraction α_{diss}. When J_{dis} = 6 kA, α_{diss} has a maximum value about 0.84 along the central axis. At J_{dis} = 13 kA, the maximum value of α_{diss} is slightly increased up to 0.88 along the central axis. In both cases, α_{diss} is gradually decreased in a radial direction, but it recovers near the anode, which is caused by high temperature near the wall due to the viscous effect.

Figure 4 shows the distribution of ionization fraction α. When J_{dis} = 6 kA, the maximum value of α reaches about 0.8 near the cathode tip (z = 50 mm, r = 0 mm). In the downstream region, however, the ionization fraction decreases from 0.80 (at the cathode tip) to 0.52 (at the thruster exit) along the central-axis, which indicates

recombination processes occur. The flow velocities at J_{dis} = 6 kA and 13 kA reach 26 km/s and 46 km/s at the thruster exit (z = 140 mm, r = 0 mm), respectively. On the other hand, in the case of J_{dis} = 13 kA, ionization fraction increases in the whole region, although the plasma is not fully ionized. In Fig. 5, the calculated ionization fraction along the symmetrical axis is compared with that determined by Saha equation (α_{saha})[10]:

$$\frac{\alpha_{saha}^2}{1-\alpha_{saha}^2} = 6.65\times10^{-2}\frac{T_e^{5/2}}{p}\exp\left(-\frac{11600(V_{diss}+V_{ion})}{T_e}\right) \tag{16}$$

In the Fig. 5, the calculated ionization fraction is kept constant (~ 0.86) along the central-axis. On the other hand, α_{saha} reach fully ionization from the cathode tip to z = 100 mm (z = 110 mm in the case of V_{diss} = 0 eV for Eq.(16)), and in the downstream region, it decreases with temperature due to expansion of the flow. The difference between calculated and Saha equilibrium ionization fraction indicates chemical non-equilibrium. In addition, the time for the recombination $\tau_{\text{recomb.}}$ and the flow characteristic time τ_{flow} are evaluated as follows:

$$\tau_{recomb.} = \frac{\rho}{\dot{\rho}_{H^+}} = \frac{\rho}{\left|m_{H^+}k_{IB}n_{H^+}n_e n_e\right|} \tag{17}$$

$$\tau_{flow} = \frac{z}{u} \tag{18}$$

At the thruster exit (z = 140 mm, r = 0 mm), $\tau_{\text{recomb.}}$ (0.758 ms) is much longer than τ_{flow} (3.05 μ s). Consequently, the plasma flow out before recombination occurs.

Figure 6 shows the distribution of the electron number density. A high number density (~ 1.6×10^{22} m^{-3}) region is observed on the side of the cathode due to the pinching force (radial Lorentz force) at J_{dis} = 6 kA. When J_{dis} = 13 kA, the highest number density (~ 6×10^{22} m^{-3}) region is located at the cathode surface (around z = 12 mm) due to the high total density which is caused by the compression wave.

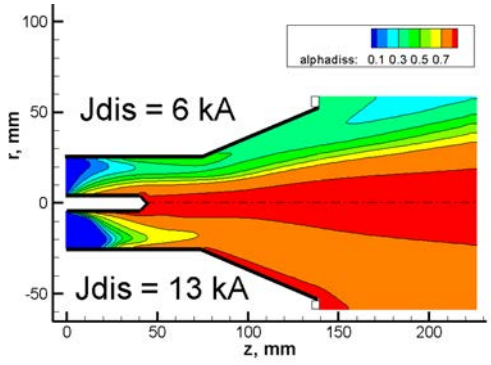

Figure 3. Dissociation Fraction (H_2, $\dot{m}$ = 1.37 g/s).

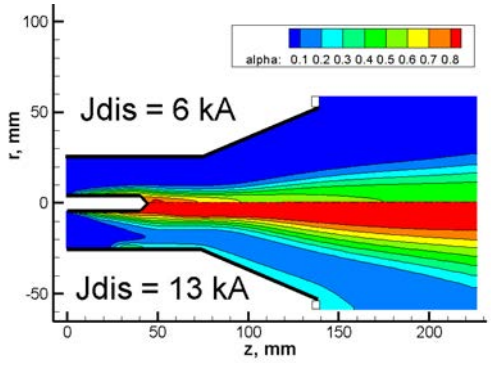

Figure 4. Ionization Fraction (H_2, $\dot{m}$ = 1.37 g/s)

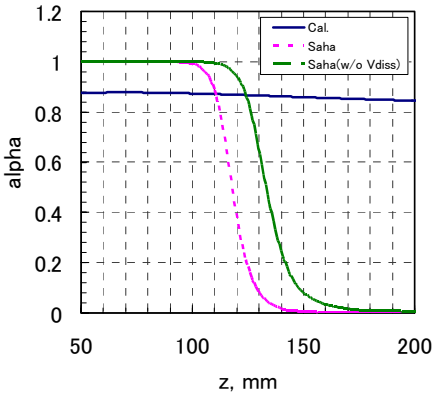

Figure 5. Ionization fraction along the symmetrical axis (Comparison between Calculated and Saha equation, H_2, $\dot{m}$ = 1.37 g/s, J_{dis} = 13 kA).

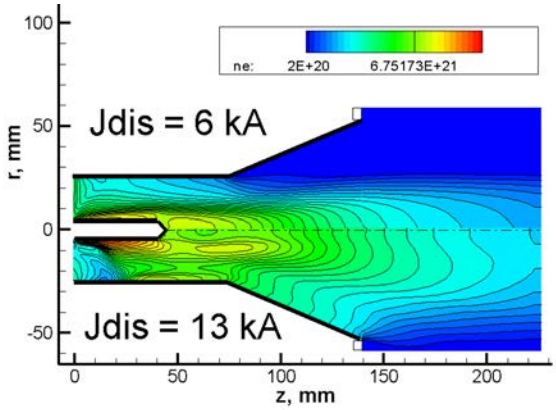

Figure 6. Electron Number Density, m^{-3} (H_2, $\dot{m}$ = 1.37 g/s).

Pressure

The pressure (= $p_h + p_e$) is shown in Fig. 7. When J_{dis} = 6 kA, the pressure decreases in the downstream direction. On the other hand, in the case of J_{dis} = 13 kA, a skewed compression wave (white dash-line in Fig. 7) extends from the cathode root and the cathode tip. The compression wave from the cathode root is reflected from the anode surface to central-axis. Then, the plasma flow reaches supersonic in the upstream region of skewed compression wave from the cathode root. The compression wave was also observed in the numerical simulation for the other thruster geometry with argon and hydrogen propellant [4,5].

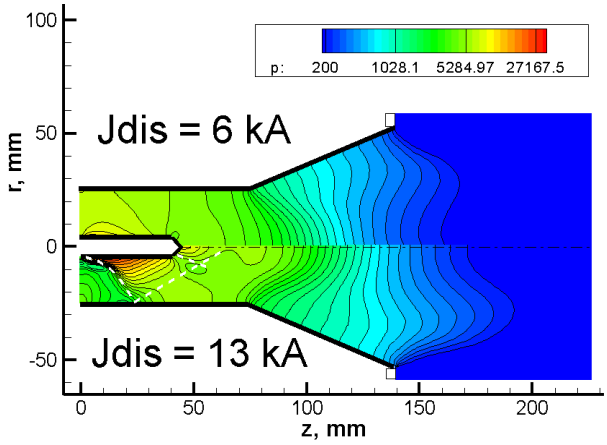

Figure 7. Pressure, Pa (H_2, $\dot{m}$ = 1.37 g/s).

Temperature

Figure 8 shows the electron temperature. When J_{dis} = 6 kA, the maximum value of T_e is 1.4 eV at the cathode tip. On the other hand, in the case of J_{dis} = 13 kA, the maximum value of T_e is 3.8 eV at the cathode root and tip. Additionally, the ratio of electron temperature to heavy particle temperature (T_e/T_h) is shown in Fig. 9. In the case of both J_{dis} = 6 kA and 13 kA, thermal equilibrium ($T_e/T_h \sim 1$) is reached in almost whole region. The region near the cathode root becomes thermally non-equilibrium ($T_e > T_h$) due to high discharge current density (90%) which selectively heats the electrons (Joule heating).

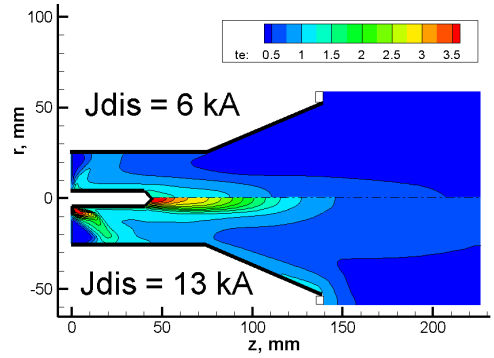

Figure 8. Electron Temperature, eV (H_2, $\dot{m}$ = 1.37 g/s).

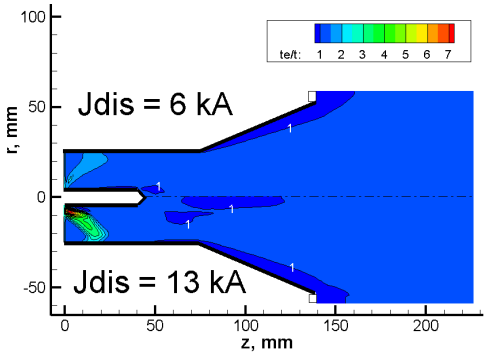

Figure 9. Ratio of Electron Temperature to Heavy Particle Temperature (H_2, $\dot{m}$ = 1.37 g/s).

B. Thrust Performance and Current-Voltage Characteristic

Thrust F is evaluated at the thruster exit as follows.

$$F = \int_{exit} \left(\rho u_z^2 + p \right) dA_{exit} \tag{19}$$

The calculated and the measured thrust[1] are shown in Fig. 10. In the figue, the solid curve and the dashed curve show the minimum and maximum theoretical electromagnetic thrust, respectively. The calculated thrust is almost the same as the measured thrust As is well-known, thrust component is divided into the electromagnetic thrust and gasdynamic thrust. The ratio of electromagnetic thrust F_{em} (blowing force) to total thrust increases from 22.0% (J_{dis}= 5 kA) to 43.0% (J_{dis} = 8 kA). For J_{dis} > 8 kA, F_{em}/F is larger than 50% and the maximum F_{em}/F is 73.3% at J_{dis} = 13 kA.

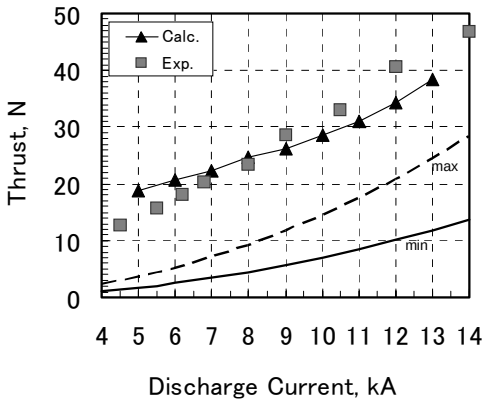

Figure 10. Discharge Current vs. Thrust (H_2, $\dot{m}$ = 1.37 g/s).

The discharge voltage V is given by a line integration of the electric field between the anode and the cathode:

$$V = \int_a^c \left(\frac{\mathbf{j}}{\sigma} - \mathbf{u} \times \mathbf{B} + \frac{1}{en_e} \mathbf{j} \times \mathbf{B} \right) \cdot dl \tag{19}$$

The current-voltage characteristic is shown in Fig. 11. The voltage linearly increases with the discharge current ($V \propto J$) in the range of J_{dis} = 5 kA – 9 kA which indicates the acceleration mode is electrothermal (almost input power is input into the Joule heating). On the other hand, in the case of above J_{dis} = 8 kA, the trend around $V \propto J^3$ gives an evidence of electromagnetic thrust production. Figure 12 shows the percentage of each term (1st-3rd term) in

Eq. (19). The first term in Eq. (19) (the Joule heating) is dominant term (> 50%) in the range of J_{dis} = 5 kA – 12 kA. However, the first term decreases rapidly for J_{dis} > 12 kA, and then the second term in Eq. (19) (Back-EMF) reaches 30% at J_{dis} = 13 kA. Note that the third term in Eq. (19) (the Hall effect) becomes dominant (~ 50%) at J_{dis} = 13 kA.

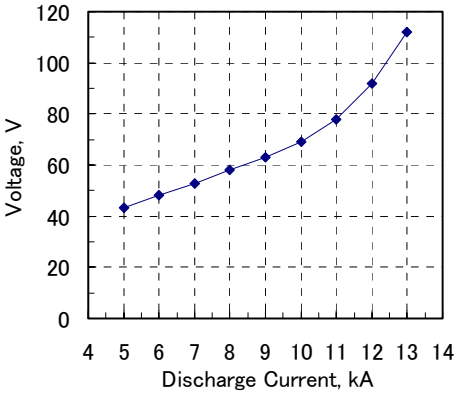

Figure 11. *J-V* Characteristic (H_2, $\dot{m}$ = 1.37 g/s).

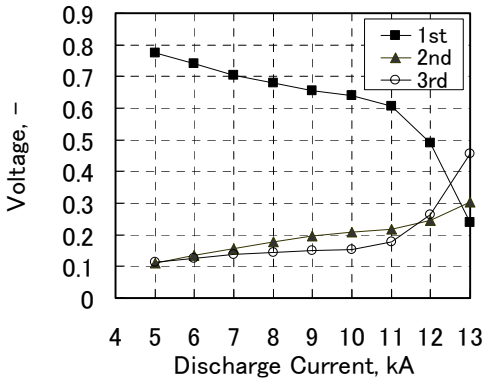

Figure 12. Components of Voltage (H_2, $\dot{m}$ = 1.37 g/s).

Typical thrust performance in the electrothermal and electromagnetic is described in Table 2. Thrust efficiency η is evaluated as follows.

$$\eta = \frac{F^2 - F_{in}^2}{2\dot{m}J_{dis}(V + V_{sh})} \tag{20}$$

Here, the sheath voltage V_{sh} is assumed equivalent to the sum of the ionization and dissociation energy (= 18 V). When V_{sh} = 18 V, the thrust efficiency is almost the same as the measured thrust efficiency.

Table 2 Typical thrust performances（H_2, $\dot{m}$ = 1.37 g/s）

	Electrothermal	Electromagnetic
J_{dis}, A	6	13
P, kW	289.2	1,454
F, N	20.8	38.5
I_{sp}, sec	1576	2856
F/P, mN/kW	71.9	26.5
η, % (V_{sh} = 0 V)	22.0	33.5
η, % (V_{sh} = 18 V)	16.0	28.8

C. Characteristic of Discharge Current

The current contour lines can be obtained by the current stream function ϕ .

$$\psi \equiv rB_\theta \tag{21}$$

Figure 13 shows the discharge current path. When J_{dis} = 6 kA, the discharge current uniformly flows into the cathode. In the case of J_{dis} = 13 kA, the discharge current expands toward the downstream on the anode surface due to the Hall effect, which is caused enhanced both by both an increase in the induced self-magnetic field and by an decrease in the number density. When J_{dis} = 13 kA, the Hall parameter reaches the maximum value about 1.7 on the straight region of the anode (z = 16 mm), whereas the Hall parameter on the same point for J_{dis} = 6 kA is around 0.22.

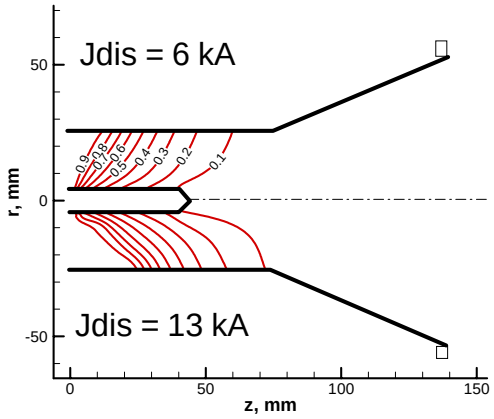

Figure 13. Discharge current path (H$_2$, $\dot{m}$ = 1.37 g/s, label shows ϕ)

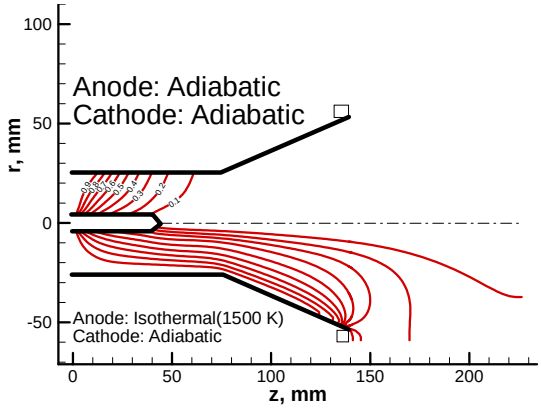

Figure 14. Current Path (H$_2$, $\dot{m}$ = 1.37 g/s, J_{dis} = 10 kA, label shows ϕ, $J^2/\dot{m}$ = 73.0 kA^2/g/s)

In order to compare the calculated current path with the experimental results[6] under almost the same $J^2/\dot{m}$, the current contour lines for 10 kA is shown in Fig. 14($J^2/\dot{m}$ =73.0 kA^2/g/s in this simulation, and 62.5 kA^2/g/s in the experiment). Figure 14 shows the current path in the case of J_{dis} = 10 kA ($J^2/\dot{m}$ = 73.0 kA^2/g/s). In the upper half of Fig. 14, for which the adiabatic condition is imposed on both electrodes, the current flows diffusively, but this disagrees with the experimental result. This disagreement may be caused by the boundary condition on the anode. In the lower half of Fig. 14, for which the isothermal condition (T_h = T_e = 1500 K) is imposed on the anode surface in order to take into account anode heat losses, the current path expands toward the thruster exit. This tendency can also be seen from the experimental result. On the anode, most of the current (80%) concentrates on the anode edge due to the Hall effect.

The current path influences on the structure of a cathode jet. Figure 15 shows the ionization fraction in the case of J_{dis} = 10 kA under the both boundary conditions. Adopting the isothermal condition on the anode, a cathode jet with the high ionization fraction (~0.95) is produced, whereas recombination processes seems to occur in the cathode jet under the adiabatic boundary condition on the anode.

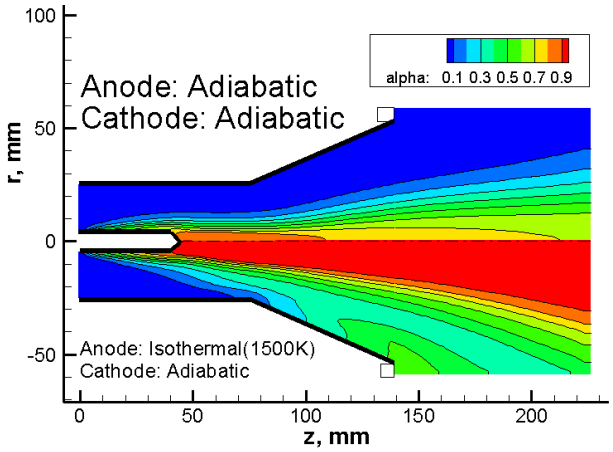

Figure 15.Ionization fraction (H$_2$, $\dot{m}$ = 1.37 g/s, J_{dis} = 10 kA).

D. Energy Balance

The energy fluxes at thruster exit are evaluated under adiabatic boundary condition as follows.

$$E_{kinetic} = \int_{exit} \frac{1}{2} \rho \left(u_z^2 + u_r^2 \right) u_z dA_{exit} \tag{22}$$

$$E_{tr} = \int_{exit} \frac{3}{2} p u_z dA_{exit} \tag{23}$$

$$E_{press} = \int_{exit} p u_z dA_{exit} \tag{24}$$

$$E_{diss} = \int_{exit} \frac{1}{2} n_H \hat{V}_{diss} u_z dA_{exit} \tag{25}$$

$$E_{ion} = \int_{exit} n_e \left(\frac{1}{2} \hat{V}_{diss} + \hat{V}_{ion} \right) u_z dA_{exit} \tag{26}$$

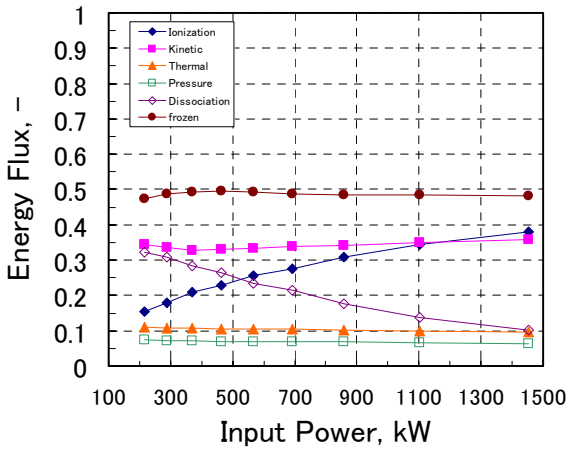

Figure 16. Input Power vs. Normalized Energy Fluxes (H_2, $\dot{m}$ = 1.37 g/s, J_{dis} = 5 kA – 13 kA).

Here, the subscripts "kinetic", "tr", "press", "diss", and "ion" denote kinetic, thermal, pressure, dissociation, and ionization energy flux, respectively. The sum of E_{diss} and E_{ion} can be interpreted as the frozen flow loss E_{frozen}. Figure 16 shows the percentage of each energy flux which is normalized by the sum of an injected energy E_{in} from the inlet and the input power. $E_{kinetic}$ increases with the input power in the case of above J_{dis} = 7 kA. On the other hand, E_{diss} decreases with increasing the input power. In contrast, E_{ion} increases with the input power. Additionally, E_{frozen} (=E_{diss} + E_{ion}) decreases with increasing the input power in the case of above P = 464 kW (J_{dis} = 8 kA). E_{frozen} is dominant energy (~ 50%) flux regardless of the input power. In addition, E_{tr} and E_{press} achieve around 10% and around 7% regardless of the discharge current, respectively. The percentage of the frozen flow (~50%) is larger than that (~ 24%) of other study. [2,12] The reason for this may be that rotational and vibrational energies are ignored in the simulation.

IV. Conclusion

The numerical simulation of plasma flow in an MPD thruster with hydrogen propellant has been conducted in consideration of realistic effects (e.g. thermal nonequilibrium, dissociation-ionization process, and the Hall effect). In this study, the flow field, characteristic of the discharge current, and the energy balance are examined. The results are summarized as follows.

- The plasma flow is neither fully dissociated nor fully ionized even (the maximum value for the dissociation and ionization fraction is equal to ~ 0.88 and 0.87, respectively) due to chemical non-equilibrium, although the dissociation and ionization fraction increases with the discharge current. The recombination hardly occurs in the downstream region.

- The calculated thrust is almost the same as the experimental thrust in almost range of discharge current (216 kW-1.45 MW, F = 18.9 – 38.5 N, I_{sp} = 1443 - 2856 sec).

- The discharge current path expands to downstream on the anode due to the Hall effect with increasing discharge current. In addition, in the case of closing $J^2/\dot{m}$, the current path tend to expand to the downstream which is similar to the measured current path under the isothermal condition for temperature on the anode surface.

- From the analysis of energy flux of the ejected plasma flow, the frozen flow loss is dominant energy flux regardless of the input power.

Appendix

We describe the transport property for the simulation in this appendix.

Thermal Conductivity

Thermal conductivity of heavy particle λ_h is evaluated as follows.

$$\lambda_h = 0.45\frac{R_{ave}}{\gamma-1}\sqrt{\frac{\pi}{2}}\sqrt{2m_{ave}kT_h}\sum_{s\neq e}\frac{n_s}{n_e Q_{es}\sqrt{T_e/T_h}\sqrt{2m_e/m_s}+\sum_{j\neq e}n_j Q_{sj}} \tag{A.1}$$

Here, R_{ave} and m_{ave} correspond to the average of gas constant and particle mass, respectively. Q_{ij} means the collision cross section between *i* and *j* species.

$$R_{ave} = \frac{\rho_{H_2}}{\rho}R_{H_2}+\frac{\rho_H}{\rho}R_H+\frac{\rho_{H^+}}{\rho}R_{H^+} \tag{A.2}$$

$$m_{ave} = \frac{\rho_{H_2}}{\rho}m_{H_2}+\frac{\rho_H}{\rho}m_H+\frac{\rho_{H^+}}{\rho}m_{H^+} \tag{A.3}$$

Additionally, thermal conductivity of electron λ_e is evaluated as follows.

$$\lambda_e = 2.8\sqrt{\frac{\pi}{2}}\frac{n_e k^2 T_e}{\sqrt{m_e kT_e}\left(n_e Q_{ee}+\sum_{s\neq e}n_s Q_{es}\right)} \tag{A.4}$$

Viscosity Coefficient

The viscosity coefficient μ is evaluated as follows.

$$\mu = \frac{\lambda_h(\gamma-1)}{R_{ave}} \tag{A.5}$$

Here, Prandtl number is set to 1.0.

Electric Conductivity

Electric conductivity σ is evaluated as follows.

$$\sigma = \frac{e^2 n_e}{m_e \nu_{eh}} \tag{A.6}$$

Here, ν_{eh} means the collision frequency.

$$\nu_{eh} = \left(n_{H_2}Q_{eH_2}+n_H Q_{eH}+n_{H^+}Q_{eH^+}\right)\sqrt{\frac{8kT_e}{\pi m_e}} \tag{A.7}$$

Acknowledgments

This work is supported by the Center for Planning and information Systems in Institute of Space and Astronautical Science.

References

[1] Tahara, H., Kagaya, Y., and Yoshikawa, T., "Quasi-Steady MPD Arcjets with Applied Magnetic Fields," *18th International Electric Propulsion Conference*, Virginia, 1985, AIAA-85-2001.

[2] Mikellides, P.G., "Modeling and Analysis of a Megawatt-Class Magnetoplasmadynamic Thruster," *Journal of Propulsion and Power*, Vol. 20, No.2, 2004, pp.204-210.

[3] Shoji, T., and Kimura, I., "Analytical Study on the Influence of Nonequilibrium Ionization for Current Flow Pattern and Flow Field of MPD Arcjets," *21st International Electric Propulsion Conference*, Orland, 1990, AIAA-90-2609.

[4] Kubota, K., Funaki, I., and Okuno, Y., "Numerical Study of Plasma Behavior in a Magnetoplasmadynamic Thruster Around Critical Current," *Journal of Propulsion and Power*, Vol.25, No.2, 2009, pp.397-405.

[5] Sato, H., Kubota, K., and Funaki, I., "Numerical Simulation of a Self-Field Magnetoplasmadynamic Thruster with Hydrogen Propellant," *17th International Conference on MHD Energy Conversion*, Kanagawa, Japan, 2009.

[6] Tahara, H., Yasui, H., Kagaya, Y., and Yoshikawa, T., "Experimental and Theoretical Researches on Arc Structure in a Self-Field Thruster," *19th International Electric Propulsion Conference*, Colorado, 1987, AIAA-87-1093.

[7] Anderson, J.D., *Hypersonic and High-Temperature Gas Dynamics*, Amer Inst of Aeronautics, 2006.

[8] Mitsuo, K., Tahara, H., Kiumra, T., Kagaya, Y., and Yoshikawa, T., "ARC STRUCTURE IN A COAXIAL MAGNETOPLASMADYNAMIC CHANNEL," *26th International Electric Propulsion Conference*, 1999, IEPC-99-179.

[9] Kuchi-ishi, S., "Numerical Studies of Thermochemical Nonequilibrium Flows in a DC Arcjet Thruster," Doctor thesis, 1999.

[10] Kuriki, K., *Introduction to Electric Propulsion*, University of Tokyo Press, 2003.

[11] Tahara, H., Kagaya, Y., and Yoshikawa, T., "Arc Structure in a Quasi-Steady MPD Thruster," *JSASS*, Vol. 33, No. 382, 1985.

[12] Kiyoshi, K., Toki, K., and Funaki, I., "Nozzle Shape Effect on Velocity Distribution in an MPD Arcjet," *28st International Electric Propulsion Conference*, Toulouse, France, 2003, IEPC-03-0056.

[13] Sankaran, K., Choueiri, E. Y., and Jardin, S. C., "Comparison of Simulated Magnetoplasmadynamic Thruster Flowfields to ExperimentalMeasurements," *Journal of Propulsion and Power*, Vol. 21,No. 1, 2005, pp. 129–138.

[14] Heiermann, J., and Auweter-Kurtz, M., "Numerical and ExperimentalInvestigation of the Current Distribution in Self-Field Magnetoplasmadynamic Thrusters," *Journal of Propulsion and Power*, Vol. 21,No. 1, 2005, pp. 119–128.

[15] Niewood, E. H., and Martinez-Sanchez, M., "The Hall Effect in a Numerical Model of MPD Thrusters," 22nd International Electric Propulsion Conference, Paper 91-099, Oct. 1991.

[16] Choueiri, E. Y., and Ziemer, J. K., "Quasi-Steady Magnetoplasmadynamic Thruster Performance Database," *Journal of Propulsion and Power*, Vol. 17, No.5, pp.967-976, 2001.

[17] Kuriki, K., Uematsu, K., and Morimoto, S., "MPD Arcjet Performance with Various Propellants," *16th International Electric Propulsion Conference*, Louisiana, 1982, AIAA-82-1885.

[18] Tahara, H., Sakakibara, T., Kagaya, Y., and Yoshikawa, T., "Operational Characteristics and Discharge Mechanism of Quasisteady Magnetoplasmadynamic (MPD) Arcjet for Space Propulsion," *Journal of Plasma and Fusion Research*, Vol. 8, No.195, 1990. (in Japanese)

[19] Auweter-Kurtz, M., and Messerschmid, E., "Plasma Accelerator Activities at the IRS," *21st International Electric Propulsion Conference*, Orland, FL, 1990, AIAA-90-2659.

[20] Sumida, M., and Toki, K., "Real-Gas Effect on the Magnetoplasmadynamic Arcjet," *Journal of Propulsion and Power*, Vol. 7, No. 6, 1991, pp. 1072–1074.

[21] I. Funaki, K. Toki, and K. Kuriki, "Nonequilibrium Flow Analysis of a Two-dimensional MPD Arcjet," *25st International Electric Propulsion Conference*, Ohio, 1997, pp. 699-704, IEPC-97-112.

[22] Gnoffo, P. A., Gupta, R. N., and Shinn, J. L. "Conservation Equations and Physical Models for Hypersonic Air Flows in Thermal and Chemical Nonequilibrium," NASA TP 2867, 1989.